

X-Ray Absorption Analysis of MCG –6–30–15: Discerning Three Kinematic Systems

Tomer Holczer ¹, Ehud Behar ^{2,3}, and Nahum Arav ⁴

ABSTRACT

By analyzing the X-ray spectrum of MCG –6–30–15 obtained with the HETGS spectrometer on board the *Chandra* observatory, we identify three kinematically distinct absorption systems; two outflow components intrinsic to MCG –6–30–15, and one local at $z = 0$. The slow outflow at $-100 \pm 50 \text{ km s}^{-1}$ has a large range of ionization manifested by absorption from 24 different charge states of Fe, which enables a detailed reconstruction of the absorption measure distribution (*AMD*). This *AMD* spans five orders of magnitude in ionization parameter: $-1.5 < \log \xi < 3.5$ ($\text{erg s}^{-1} \text{ cm}$), with a total column density of $N_H = (5.3 \pm 0.7) \times 10^{21} \text{ cm}^{-2}$. The fast outflow at $-1900 \pm 150 \text{ km s}^{-1}$ has a well defined ionization parameter with $\log \xi = 3.82 \pm 0.03$ ($\text{erg s}^{-1} \text{ cm}$) and column density $N_H = 8.1 \pm 0.7 \times 10^{22} \text{ cm}^{-2}$. Assuming this component is a thin, uniform, spherical shell, it can be estimated to lie within 11 light days of the AGN center. The third component, most clearly detected in the lower oxygen charge states $\text{O}^{+1} - \text{O}^{+6}$, has been confused in the past with the fast outflow, but is identified here with local gas ($z = 0$) and a total column density N_H of a few 10^{20} cm^{-2} . Finally, we exploit the excellent spectral resolution of the HETGS and use the present spectrum to determine the rest-frame wavelengths of oxygen inner-shell lines that were previously uncertain.

Subject headings: galaxies: active — galaxies: individual (MCG –6–30–15) — techniques: spectroscopic — X-rays: galaxies — line: formation

¹Department of Physics, Technion, Haifa 32000, Israel. tomer@physics.technion.ac.il (TH), behar@physics.technion.ac.il (EB).

²Code 662, NASA / Goddard Space Flight Center, Greenbelt, MD 20771, USA

³Senior NPP Fellow on leave from the Technion, Israel

⁴Department of Physics, Virginia Tech, Blacksburg, Va 24061. arav@vt.edu

1. INTRODUCTION

Approximately half of type 1 AGNs show complex absorption in the soft X-ray band (Crenshaw et al. 2003). The blue shifted absorption lines come from a highly or partly ionized outflow first noted by Halpern (1984). These outflows may play a central role in cosmological feedback, in the metal enrichment of the intergalactic medium (IGM) and in understanding black hole evolution. However, the outflow physical properties such as mass, energy and momentum are still largely unknown. A necessary step to advance on these issues is to obtain reliable measurements of the ionization distribution, and column densities of the outflowing material.

MCG –6–30–15 is a bright Seyfert 1 galaxy ($L_X \sim 10^{43}$ erg s $^{-1}$) at a redshift $z = 0.007749$ (Fisher et al. 1995). It shows strong optical reddening (Reynolds et al. 1997), which suggests that the absorber may also contain some cold (neutral) gas. MCG –6–30–15 is a highly variable X-ray source with changes up to a factor of 2 on time scales of ~ 1 ks (Fabian et al. 1994; Reynolds et al. 1995; Otani et al. 1996) MCG –6–30–15 is well known for its relativistically broadened emission feature at 5 – 7 keV (Tanaka et al. 1995; Ballantyne et al. 2003; Young et al. 2005) that has been interpreted as Fe K α emission from the accretion disk deep inside the black hole gravitational potential well.

There are numerous studies in the literature of the ionized X-ray absorber of MCG –6–30–15 the most important of which are listed in Table 1. Otani et al. (1996) analyzed the *ASCA* data and Reynolds et al. (1997) fitted the *ROSAT* and *ASCA* spectra using strong, variable, oxygen absorption edges to explain the curved continuum shape. In 2000, Branduardi-Raymont et al. (2001) obtained the first grating spectra of MCG –6–30–15 with the Reflection Grating Spectrometer (RGS) on board *XMM-Newton*. The improved resolution showed the spectral turn overs to be inconsistent with the oxygen edge positions. Indeed, Branduardi-Raymont et al. (2001) modeled the soft X-ray spectrum with relativistic emission lines from deep in the accretion disk of C $^{+5}$, N $^{+6}$ and O $^{+7}$, instead of absorption edges. Lee et al. (2001) then used the 2000 *Chandra* High Energy Transmission Grating (HETGS) spectrum of MCG –6–30–15 to claim that (O $^{+6}$ but mostly) neutral Fe L-shell edges can explain the continuum turn over at ≈ 17.5 Å (see also Lee et al. 2009), and not relativistic emission lines. As in previous works, Lee et al. (2001) needed two ionization zones in order to fit the soft X-ray absorption lines. Sako et al. (2003) reinstated the Branduardi-Raymont et al. (2001) interpretation of the 2000 RGS data, but with a better absorption model. Sako et al. (2003) identified two velocity components in the absorber with outflow velocities of -150 km s $^{-1}$ and -1900 km s $^{-1}$. Turner et al. (2004) fitted a second longer 320 ks RGS observation from 2001, and confirmed the two kinematic components, with (roughly consistent) velocities of $+80 \pm 260$ km s $^{-1}$ and -1970 ± 160 km s $^{-1}$. Young et al. (2005) studied a long 520 ks 2004 *Chandra* HETGS

observation, and found some of the most highly ionized species of Fe^{+24} , Fe^{+25} , S^{+15} and Si^{+13} to be outflowing at -2000 km s^{-1} . The analysis of McKernan et al. (2007) of the previous 2000 HETGS spectrum again confirmed the fast component, but with a slightly different velocity of $-1550_{-130}^{+80} \text{ km s}^{-1}$. They also reported two slow components with low velocities of $\leq 30 \text{ km s}^{-1}$ and $\leq 15 \text{ km s}^{-1}$. Recently, Miller et al. (2008) studied all of the archival spectra of MCG –6–30–15 including a 2006 *Suzaku* observation and confirmed the fast outflow and the slow outflow with its two ionization components. Miller et al. (2008) also invoked a partial covering absorber that helps explain the continuum shape without the need of relativistically broadened emission lines. Most recently, Chelouche (2008) modeled the 2004 HETGS spectrum with similar components as the previous authors. We summarize the long list of previous works on this intriguing target and in particular its grating observations by stating that while the gratings have led to unambiguous measurements of the kinematics and ionization of the absorbing outflow, the physical interpretation of the X-ray continuum is still being debated.

In this paper, we wish to further investigate the physical conditions of the MCG –6–30–15 X-ray absorber, using the archival 520 ks HETGS observation from 2004, but with special focus on the ionization distribution of the plasma, and on lines that do not seem to fit the simple two-velocity picture (see list of individual-line velocities in Turner et al. 2004). While the majority of works on the X-ray spectra of AGN outflows employ gradually increasing number of ionization components, until the fit is satisfactory (e.g., Kaspi et al. 2001; Sako et al. 2003), it is instructive to reconstruct the actual distribution of the column density in the plasma as a continuous function of ionization parameter ξ (Steenbrugge et al. 2005), which we termed the absorption measure distribution (*AMD*, Holczer et al. 2007). Although for high-quality spectra such as the present one, two or three ionization components might produce a satisfactory fit, the *AMD* reconstruction is the only method that reveals the actual distribution including its physical discontinuities (e.g., due to thermal instability), and ultimately provides a more precise measurement of the total column density.

2. DATA REDUCTION

MCG –6–30–15 was observed by *Chandra*/HETGS on 19–28 May, 2004 for a total exposure time of 520 ks. All observations were reduced from the *Chandra* archive using the standard pipeline software (CIAO version 3.2.1). The total number of counts in the first (plus and minus) orders between 2 and 20 Å is 353485 for MEG (medium energy grating) and 165698 for HEG (high energy). More details on the observation can be found in Table. 2. No background subtraction was required as the background level was negligible. Flux spec-

tra were obtained by first co-adding count spectra from the different refraction orders and convoluting with the broadest line spread function (MEG ± 1 orders) to ensure uniformity. The total count spectra were then divided by the total effective area curve (summed over orders) and observation time. Finally, spectra were corrected for neutral Galactic absorption of $N_H = 4.1 \times 10^{20} \text{ cm}^{-2}$ (Dickey & Lockman 1990).

3. SPECTRAL MODEL

Variations of approximately 40% on time scales of 20 ks were observed over the 520 ks total exposure of MCG –6–30–15. Light curves can be found in Young et al. (2005). The average flux of MCG –6–30–15 does not vary by more than 40% between maximum and minimum flux levels over the 14 years it has been observed, as can be seen from the continuum flux levels quoted in Table 1. The present work deals with the long term properties of the ionized absorber. With these small and rapid variations the absorber is not expected to significantly vary. Henceforth, we generally use the combined MEG and HEG full 520 ks spectrum that is shown in Fig. 1. At the shortest wavelengths ($\lambda < 6$), we exploit the superior spectral resolution and effective area of HEG (top panel in Fig. 1). The present fitting procedure follows our ion-by-ion fitting method (Behar et al. 2001; Sako et al. 2001; Behar et al. 2003; Holczer et al. 2005). First, we fit for the broad-band continuum. Subsequently, we fit the absorption features using template ionic spectra that include all of the absorption lines and photoelectric edges of each ion, but vary with the broadening (so-called turbulent) velocity and the ionic column density. Strong emission lines are fitted as well.

3.1. Continuum Parameters

The continuum X-ray spectrum of most AGNs can be characterized by a high-energy power-law and a soft excess that rises above the power law at lower energies below ~ 1 keV. This soft excess is often modeled with a blackbody, or modified blackbody, although it clearly is more spectrally complex and possibly includes prominent atomic features. MCG –6–30–15 can not be properly fitted by such a simplistic model because of a sharp jump in flux at $\sim 17.5 \text{ \AA}$. As explained in §1, there is a controversy regarding how to interpret this sharp spectral feature; One model (Branduardi-Raymont et al. 2001; Sako et al. 2003) uses relativistically broadened emission lines, while the other option is to invoke a steep soft excess (Lee et al. 2001) that is then absorbed by a large column density. In this work, given the ambiguity of the 17.5 \AA feature, and since we wish to focus on the absorption lines, we use a phenomenological cubic spline continuum, not very different from that used by Turner et al.

(2004), that characterizes the continuum flux level most adequately throughout the spectrum.

3.2. The Ionized Absorber

The intensity spectrum $I_{ij}(\nu)$ around an atomic absorption line $i \rightarrow j$ can be expressed as:

$$I_{ij}(\nu) = I_0(\nu) e^{-N_{ion}\sigma_{ij}(\nu)} \quad (1)$$

where $I_0(\nu)$ represents the unabsorbed continuum intensity, $\sigma_{ij}(\nu)$ denotes the line absorption cross section for photo-excitation (in cm^2) from ground level i to excited level j . If all ions are essentially in the ground level, N_{ion} is the total ionic column density towards the source (in cm^{-2}). The photo-excitation cross section is given by:

$$\sigma_{ij}(\nu) = \frac{\pi e^2}{m_e c} f_{ij} \phi(\nu) \quad (2)$$

where the first term is a constant that includes the electron charge e , its mass m_e , and the speed of light c . The absorption oscillator strength is denoted by f_{ij} , and $\phi(\nu)$ represents the Voigt profile due to the convolution of natural (Lorentzian) and Doppler (Gaussian) line broadening. The Doppler broadening consists of thermal and turbulent motion, but in AGN outflows, the turbulent broadening is believed to dominate the temperature broadening. The Natural broadening becomes important when the lines saturate as in our current spectrum, e.g. the O^{+6} line. Transition wavelengths, natural widths and oscillator strengths were calculated using the Hebrew University Lawrence Livermore Atomic Code (HULLAC, Bar-Shalom et al. 2001). Particularly important for AGN outflows are the inner-shell absorption lines (Behar et al. 2001; Behar & Netzer 2002). More recent and improved atomic data for the Fe M-shell ions were incorporated from Gu et al. (2006).

Since the absorbing gas is outflowing, the absorption lines are slightly blue-shifted with respect to the AGN rest frame. Although blue shifts of individual lines can differ to a small degree, we can identify two overall distinct kinematic components with best-fit outflow velocities of $v = -100 \pm 50 \text{ km s}^{-1}$ and $v = -1900 \pm 150 \text{ km s}^{-1}$. These velocities are set in the model to one value (for each component) for all of the ions. There are absorption lines mostly from oxygen in the range above $\sim 20 \text{ \AA}$, which appear even more blue shifted than -1900 km s^{-1} . These lines are addressed in detail in §4.4.

For the slow component, a turbulent velocity of $v_{\text{turb}} = 100 \text{ km s}^{-1}$ is used. The turbulent

velocity (referred to by some as the b parameter) is defined as $v_{\text{turb}} = \sqrt{2}\sigma = \text{FWHM}/\sqrt{4 \ln 2}$, where σ is the standard deviation and FWHM is the full width at half max. The value of 100 km s^{-1} , although, unresolved by HETGS, provides a good fit to the strongest absorption lines in the spectrum. For the fast component, $v_{\text{turb}} = 500 \text{ km s}^{-1}$ (FWHM = 830 km s^{-1}) is used. Since the fast component is detected mostly in highly-ionized species at short wavelengths where the grating resolving power is lowest, this value is obtained primarily from the O^{+7} Ly α line at 18.97 \AA , but fits all lines well. Finally, the model includes also the 23 m\AA instrumental broadening, which in terms of velocity (FWHM) is, e.g., 460 km s^{-1} for the Fe^{+16} resonant line at 15.01 \AA and 1115 km s^{-1} for the Si^{+13} Ly α line at 6.18 \AA . The value of $v_{\text{turb}} = 100 \text{ km s}^{-1}$ for the slow component is the same value used by Lee et al. (2001) and by Sako et al. (2003). McKernan et al. (2007) use 170 km s^{-1} , which is still just unresolved by the HETGS. The value of $v_{\text{turb}} = 500 \text{ km s}^{-1}$ for the fast component is consistent with that quoted by Young et al. (2005) and by Miller et al. (2008).

Our model includes all of the important lines of all ion species that can absorb in the waveband observed by HETGS. In the slow component of MCG –6–30–15, we find evidence for the following ions: N^{+6} , Fe^{+1} – Fe^{+23} as well as neutral iron, all oxygen states, Ne^{+3} – Ne^{+9} , Mg^{+4} – Mg^{+11} and Si^{+5} – Si^{+13} . We also include the K-shell photoelectric edges for all these ions although their effect here is largely negligible. When fitting the data, each ionic column density is treated as a free parameter. A preliminary spectral model is obtained using a Monte-Carlo fit applied to the entire spectrum. Subsequently, the final fit is obtained for individual ionic column densities in a more controlled manner, which ensures that the fit of the leading lines is not compromised. The best fit model is shown in Fig. 1. It can be seen that most ions are reproduced fairly well by the model. Note that some lines could be saturated, e.g., the leading lines of O^{+6} and O^{+7} . In these cases, the higher order lines with lower oscillator strengths are crucial for obtaining reliable N_{ion} values.

3.3. AMD Method

The large range of ionization states present in the absorber strongly suggests that the absorption arises from gas that is distributed over a wide range of ionization parameter ξ . Throughout this work, we use the following convention for the ionization parameter $\xi = L/(n_H r^2)$ in units of $\text{erg s}^{-1} \text{ cm}$, where L is the ionizing luminosity, n_H is the H number density, and r is the distance from the ionizing source. We apply the Absorption Measure Distribution (*AMD*) analysis in order to obtain the total hydrogen column density N_H along the line of sight. The *AMD* can be expressed as:

$$AMD \equiv \partial N_H / \partial(\log \xi) \quad (3)$$

and

$$N_H = \int AMD \, d(\log \xi) \quad (4)$$

The relation between the ionic column densities N_{ion} and the AMD is then expressed as:

$$N_{ion} = A_z \int \frac{\partial N_H}{\partial(\log \xi)} f_{ion}(\log \xi) d(\log \xi) \quad (5)$$

where N_{ion} is the measured ion column density, A_z is the element abundance with respect to hydrogen taken from Asplund et al. (2009) and assumed to be constant throughout the absorber, and $f_{ion}(\log \xi)$ is the fractional ion abundance with respect to the total abundance of its element. Here, we aim at recovering the AMD for MCG –6–30–15.

For the AMD , we need to find a distribution $\partial N_H / \partial(\log \xi)$ that after integration (eq. 5) will produce all of the measured ionic column densities. When fitting an AMD , one must take into account the full dependence of f_{ion} on ξ . We employ the XSTAR code (Kallman & Bautista 2001) version 2.1kn3 to calculate $f_{ion}(\log \xi)$ using a best-fit power-law and blackbody continuum extrapolated to the range of 1 – 1000 Rydberg. We assume all charge states see the same ionizing spectrum. This is justified by the absence of significant bound-free absorption edges in the spectrum. All elements are expected to reflect the same AMD distribution, due to the assumption that they all reside in the same gas. Iron however, has a special role as it covers almost five orders of magnitude in ξ , more than any other element. More details on the AMD binning method and error calculations can be found in Holczer et al. (2007). Further physical implications emanating from AMD analysis of Seyfert outflows can be found in Behar (2009, submitted).

3.4. Narrow Emission Lines

The present MCG –6–30–15 spectrum has a few narrow, bright emission lines of Fe, Ne, and O, which are assumed not to be absorbed by the outflow, but are absorbed by the local component discussed in §4.4 (and by the neutral Galactic column). These lines are fitted with simple Gaussians and are found to be stationary to within $\approx 70 \text{ km s}^{-1}$. The Fe $K\alpha$ blends appear slightly broader (FWHM = 15 mÅ) than the Ne and O lines

whose widths are consistent with a kinematic broadening of 235 km s^{-1} FWHM, as expected for features comprised of many lines from several charge states. The centroid wavelength and photon flux are measured for each feature and listed in Table 3. The $K\alpha$ emission by neutral Fe, or generally M-shell Fe ions, is detected at 1.94 \AA (6.4 keV). Weaker $K\alpha$ emission from more highly ionized L-shell Fe is detected at somewhat shorter wavelengths. Both of these are likely due to a moderately ionized medium excited by the continuum. The Ne^{+8} $K\alpha$ forbidden line at 13.7 \AA is less prominent, but can still be detected. The O^{+6} $K\alpha$ forbidden and intercombination lines at 22.1 \AA , and at 21.8 \AA , respectively, are clearly detected. Conversely, the He-like *resonance* $K\alpha$ lines of Ne and O are not observed in emission. We believe these emission lines do exist since they are implied by the other He-like lines. However, because they overlap with the absorption lines from the slow outflow (§4.2) they cannot be detected. This in turn means we underestimate the absorption lines in these troughs. Kinematically therefore, the narrow emission lines might originate in the slow outflow. Narrow X-ray emission lines have been associated with the absorbing outflows in Seyfert galaxies based on the similar velocities, charge states, and column densities deduced for the emitting and absorbing plasma (Kinkhabwala et al. 2002; Behar et al. 2003) . Note that no emission lines from the fast component of -1900 km s^{-1} (§4.3) are detected. In fact, strongly blue shifted narrow emission lines are never detected, neither in the X-ray nor the UV, while slow winds of a few 100 km s^{-1} do produce narrow emission lines. Broad (2000 km s^{-1}) emission lines that might be expected if the fast component is quasi-spherically symmetric are also not observed and in any case not expected for low charge states, as the fast component is very highly ionized, as discussed below. All this seems to hint at the different physical nature (e.g., opening angle and mass) of fast and slow outflows.

The non-shifted positions ($\Delta v < 70 \text{ km s}^{-1}$) and widths (FWHM $< 250 \text{ km s}^{-1}$) of the X-ray narrow emission lines are also consistent with that of the bright, forbidden O^{+2} optical narrow emission lines at 4959 \AA and 5007 \AA , suggesting that perhaps the X-ray line emitting region is in the optical narrow line region (NLR). The higher ionization optical (coronal) lines of ionized Fe appear to be much broader (FWHM $\approx 2000 \text{ km s}^{-1}$, Reynolds et al. 1997), placing them closer to the nucleus. However, one has to wonder how robust these widths really are, given how faint these lines are in MCG –6–30–15 (see Fig. 2 in Reynolds et al. 1997).

4. RESULTS

4.1. Ionic Column Densities

The best-fit ionic column densities are listed in Table 4 and the resulting model is plotted over the data in Fig. 1. The Errors for the ionic column densities were calculated in the same manner as in Holczer et al. (2007). For the most part, the column densities in the slow component (-100 km s^{-1}) of the Fe, Si, N, Ne, and Mg ions are of the order of $10^{16} - 10^{17} \text{ cm}^{-2}$, while those of the more abundant O ions are higher and reach $\sim 10^{18} \text{ cm}^{-2}$. Comparing our results with those of Sako et al. (2003), we find that Fe L-shell, Si K-shell, Mg K-shell, Ne K-shell, and N K-shell column densities are more or less consistent. However, our oxygen ionic column densities are higher than those of Sako et al. (2003). We suspect this may be due to the better sensitivity to weak absorption lines in the particularly high signal to noise ratio (S/N) of the present spectrum. Lee et al. (2001) obtained still higher O^{+5} and O^{+6} column densities. This could be a consequence of their need to fit the 17.5 \AA drop with an O^{+6} edge. For similar reasons, we obtain a lower neutral Fe column density than Lee et al. (2001). The O^{+7} column density of Lee et al. (2001), on the other hand, is comparable to the present value.

More significant differences occur for the fast component (-1900 km s^{-1}). The current Fe K-shell column densities are slightly higher, but still consistent with those of Young et al. (2005), who used the exact same data set. On the other hand, Sako et al. (2003) using the RGS found a fast absorption component for the Fe L-shell, Ne K-shell, Mg^{+10} , Si^{+12} , and O ions, where we find only a slow component. We find the fast component exclusively in very high ionization species. For O, only O^{+7} has a fast component. What may have been identified by Sako et al. (2003) as high-velocity, low-ionization O, we ascribe to local ($z = 0$) intervening gas (see §4.4), whose apparent velocity in the reference frame of MCG $-6-30-15$ ($z = 0.007749$) would be -2320 km s^{-1} . This velocity is sufficiently close to that of the fast absorber (-1900 km s^{-1}) for the two systems to be confused by the RGS, which has lower resolving power than the presently used HETGS. The origin and location of the fast, high-ionization component is further discussed in §4.3.

4.2. AMD For The Slow Component

The best-fit *AMD* for the slow -100 km s^{-1} absorber in MCG $-6-30-15$ is presented in Fig. 2 and the integrated column density is presented in the bottom panel of Fig. 2. This *AMD* was obtained using all of the 24 charge states of Fe from neutral through Fe^{+23} . K-shell Fe is not observed for the slow component and many M-shell ions are only tentatively

detected. The *AMD* features a statistically significant minimum at $0.5 < \log \xi < 1.5$ ($\text{erg s}^{-1} \text{ cm}$), which corresponds to temperatures $4.5 < \log T < 5$ (K). A similar minimum at the same temperatures was also observed in IRAS 13349+2438, NGC 3783 (Holczer et al. 2007) and NGC 7469 (Blustin et al. 2007). It is mostly a manifestation of the relatively low ionic column densities observed for the ions Fe^{+11} – Fe^{+15} , as can be seen in Table 4. One way to explain this gap is that this temperature regime is thermally unstable (Holczer et al. 2007). Gas at $4.5 < \log T < 5$ (K) could be unstable as the cooling function $\Lambda(T)$ generally decreases with temperature in this regime (e.g., Krolik et al. 1981). Such instabilities could result in a multi phase (hot and cold) plasma in pressure equilibrium, as suggested by Krolik et al. (1981), and as recently modelled in detail by Gonçalves et al. (2007). Alternatively, the two distinct ionization regimes can be ascribed to two geometrically distinct regions along the line of sight, a high ionization region and a low ionization region, both which have their own narrow *AMD* distribution (i.e., well defined ξ). However, the fact that both components appear to have the same outflow and turbulent velocities leads us to prefer the co-spatial two-phase picture at the moment. Note that MCG –6–30–15 has an even more highly ionized component, but with a significantly higher outflow velocity of $\sim 1900 \text{ km s}^{-1}$. This component probably does come from another region in the AGN and is discussed further in §4.3.

The putatively unstable region is also avoided by the two-component model of McKernan et al. (2007). Sako et al. (2003) actually do find ions between $0.5 < \log \xi < 2$ ($\text{erg s}^{-1} \text{ cm}$). However, their model does not necessarily preclude a gap within that range. The model of Lee et al. (2001) has the low ionization component of the slow wind $\log \xi = 0.7$ $\text{erg s}^{-1} \text{ cm}$, which on the face of it falls in the unstable gap. However, that model was calculated with the CLOUDY code, while both the present work and McKernan et al. (2007) use XSTAR. The unstable region, is known to be very sensitive to the atomic data and plasma conditions (Hess et al. 1997; Chakravorty et al. 2009). The two ionization components of McKernan et al. (2007) are plotted in Fig. 2 over the presently derived *AMD*. That model of course does not provide a distribution, but rather two ξ components. Nevertheless, for the purpose of the plot, we ascribe widths of $0.3 \text{ erg s}^{-1} \text{ cm}$ to those components, which are the 3σ quoted errors on the $\log \xi$ values. It can be seen that the model of McKernan et al. (2007), or any other two component model for that matter, can account for some of the *AMD* distribution, but clearly does not realize the full range of ionization. The *total* column densities N_H from both approaches (bottom panel of Fig. 2) are formally in agreement, although the two-component model tends to overestimate the N_H as it needs to produce sufficient ion abundances far from their maximum-formation temperatures. The current integrated *AMD* of the absorber in MCG –6–30–15 (Fig. 2) gives a total column density of $N_H = (5.3 \pm 0.7) \times 10^{21} \text{ cm}^{-2}$, compared with $(7.0 \pm 1.4) \times 10^{21} \text{ cm}^{-2}$ of McKernan et al. (2007).

In order to further compare our results with previous outflow models for MCG –6–30–15, we can formally rebin the *AMD* in Fig. 2 to two regions, one below ($\log \xi < 0.5$) and one above ($\log \xi > 1.5$) the thermal instability. The physical parameters of these two ionization regions are subsequently compared with all the other works in Table 5. It can be seen that all of the early works (Otani et al. 1996; Reynolds et al. 1997; Lee et al. 2001) obtain much too high column density as they require the model to produce the sharp 17.5 Å turnover with an oxygen absorption edge. None of the models account for the full range of ionization as the *AMD* does.

It should be stressed that there are high uncertainties in the formation temperatures (and ξ) of the Fe M-shell ions due to significant uncertainties in their dielectronic recombination rates (Netzer 2004; Badnell 2006), as well as the uncertainties of the EUV and UV ionizing continuum. This could affect the actual shape of the *AMD* for $\log \xi < 0.5$ erg s⁻¹ cm. The observed minimum or two-phase structure may consequently change slightly.

4.3. Fast High-Ionization Component

MCG –6–30–15 shows two distinct velocity components. The slow one at –100 km s⁻¹ is more prevalent in the spectrum. Only eight ions are identified for the –1900 km s⁻¹ fast component, namely Fe⁺²³, Fe⁺²⁴, Fe⁺²⁵, O⁺⁷, Mg⁺¹¹, Si⁺¹³, S⁺¹⁵, and Ar⁺¹⁷. See Table 4 for their ionic column densities. This fast highly-ionized component should not be confused with the high-ionization tail of the slow component. The *AMD* analysis presented in §3.3 refers entirely to the slow component, where both high and low ionization states are present. An *AMD* analysis for the fast component is not possible with only three Fe ions. In fact, it seems this entire component can be modeled with a single ξ value and total N_H . Indeed, we find that $\log \xi = 3.82 \pm 0.03$ erg s⁻¹ cm and $N_H = 8.1 \pm 0.7 \times 10^{22}$ cm⁻² yield the measured ionic column densities of Fe⁺²³ – Fe⁺²⁵ to within 10% and those of other elements to within 60% for O⁺⁷, 25% for Si⁺¹³, 40% for S⁺¹⁵, and a factor of 4 for Mg⁺¹¹ and Ar⁺¹⁷. We use here a turbulent velocity of $v_{\text{turb}} = 500$ km s⁻¹, which is resolved by HETGS only for $\lambda > 8$ Å. At shorter wavelengths, the resolving power of HETGS decreases, as $\Delta\lambda = 23$ mÅ (FWHM) is fixed. For consistency, we use 500 km s⁻¹ for the entire fast component, which provides a good fit and reproduces all ionic column densities with a single ξ value. The above quoted errors on ξ and on N_H come from the distribution of N_{ion} values for Fe⁺²³ – Fe⁺²⁵ derived from the single best fit ξ . The physical parameters of this fast component as well as a comparison with previous works are given in Table 6. Only those works that could identify and resolve the fast component with gratings are quoted.

It can be seen in Table 6 that all authors more or less agree on the outflow velocity,

although McKernan et al. (2007) quote a somewhat lower value. The turbulent velocity is a less obvious parameter, but as we argue above it cannot be much lower than what we use, namely $v_{\text{turb}} = 500 \text{ km s}^{-1}$. Not all authors use such a high turbulent velocity. The column density we obtain is somewhat higher than in the other works, even though it is still formally consistent with the results of Young et al. (2005) and McKernan et al. (2007). The present value of $\log \xi = 3.82 \text{ erg s}^{-1} \text{ cm}$ is in good agreement with those of Young et al. (2005); McKernan et al. (2007); Miller et al. (2008). Sako et al. (2003) and Chelouche (2008) claimed to observe Fe L-shell ions as well as other low ionization species in the fast component (see Table 4), which resulted in their lower ξ values, but we conclude that the ionization parameter of this component needs to be high, and no low ionization lines exist for it. The exclusively high-ionization state of the fast component and the contrasting broad ionization distribution (including very low, see *AMD* analysis in §4.2) of the slow component are best demonstrated by the appreciably broad ionization range of inner-shell $K\alpha$ transitions of Si and Mg featured in the compact spectral region between 6 – 10 Å (Behar & Netzer 2002). This spectral region, which in MCG –6–30–15 comprises the absorption lines of Si^{+5} through Si^{+13} and of Mg^{+5} through Mg^{+11} is depicted in Fig. 3. The lines in this limited waveband cover the significant ionization range of roughly $-1 < \log \xi < 2.5 \text{ (erg s}^{-1} \text{ cm)}$. First, it can be seen that both Si^{+13} and Mg^{+11} H-like ions have absorption lines from both the slow and fast components as manifested by their double troughs. However, while the fast component is much more prominent for Si^{+13} , the opposite is true for the less ionized Mg^{+11} . This is a sign that the fast component is weaker in the less ionized species. Second, all of the lower charge states, namely He-like and into the L-shell, of both elements have only a slow component absorption line, as can be seen by the proximity of the troughs to the rest frame wavelengths of their respective transitions labeled in Fig. 3.

The outflow velocity of the fast component (-1900 km s^{-1}) is close, but significantly different (and clearly resolved by HETGS) from the cosmological recession of MCG –6–30–15 of -2320 km s^{-1} , possibly confusing the fast component with local ionized ISM absorption. This point was already discussed by Young et al. (2005), who showed that not only are the velocities slightly different, but also the high column density measured in the fast component would require an ISM absorber three orders of magnitude larger than the size of our Galaxy. Furthermore, the high ionization of the fast component up to, e.g., Fe^{+25} and Ar^{+17} , is much higher than typically found in intergalactic absorbers. We conclude that the fast component is most likely intrinsic to MCG –6–30–15. The possible confusion of low-ionization local oxygen lines with the fast component is further discussed and clarified in §4.4.

The well defined ionization parameter found for the fast outflow suggests it may be described as a uniform, spherical, thin shell. Its high column density and ionization suggest, in turn, it could lie rather close to the central AGN source. The width of the shell can be

denoted by $\Delta r = N_H/n_H$, where n_H is the hydrogen number density. Using the definition of ξ , $n_H = L/(\xi r^2)$, and one can write $\Delta r = N_H \xi r^2/L$. Requiring now that $\Delta r < r$ leads to an upper limit on the distance from the center of $r < 10^{16} L_{43} N_{H23}^{-1} \xi_4^{-1}$ cm, or $r < 0.0093$ pc, which is about 11 light days. Above, L_{43} is the 1 – 1000 Rydberg luminosity in units of 10^{43} erg s^{-1} , ξ_4 is the ionization parameter in units of 10^4 erg s^{-1} cm, and N_{H23} is the hydrogen column density in units of 10^{23} cm^{-2} . The continuum we use in this work yields $L_{43} = 1.5$. Note that the above distance estimate is somewhat affected by the line velocity broadening used in the model. With a turbulent velocity lower than 500 km s^{-1} , the derived column density would be slightly higher, and hence the estimated distance would be slightly lower. However, as argued above, the turbulent velocity is probably not much lower than 500 km s^{-1} . The present distance of 11 light days for the fast component is roughly the same as the estimate of Miller et al. (2008, referred to there as zone 3). For comparison, this is a few times the broad line region (BLR) distance of MCG –6–30–15. The BLR distance R_{BLR} can be estimated from its correlation (Bentz et al. 2008, Fig. 5) with the 5100 Å luminosity of $\lambda L_\lambda = 1.4 \times 10^{42}$ erg s^{-1} (taken from Reynolds et al. 1997, e.g., Fig. 2) to be approximately 4 ± 2 light days. The estimated black hole mass from the H β FWHM of 2400 km s^{-1} (Reynolds et al. 1997) and eq. (5) in Kaspi et al. (2000) is $3 \times 10^6 M_\odot$ with the standard factor of 2–3 uncertainty for such estimates. The Keplerian velocity at the absorber distance of 10 light days, therefore, is roughly 1200 km s^{-1} , which is slightly higher, but still consistent within the errors with the observed line broadening of $v_{\text{turb}} = 500$ km s^{-1} (FWHM= 830 km s^{-1}).

The mass outflow rate \dot{M} in the fast component can also be estimated within this thin-shell constant-density approximation. The product of the particle flux in the wind $n_H v_{\text{out}}$, the cross section of the absorbing shell Ωr^2 assuming conical geometry, and the average particle mass μm_H yields

$$\dot{M} = n_H v_{\text{out}} \Omega r^2 \mu m_H = \frac{L v_{\text{out}} \Omega \mu m_H}{\xi} \quad (6)$$

where v_{out} is the outflow velocity (–1900 km s^{-1} here) and Ω is the unknown opening solid angle of a presumably conical flow. For the right hand side of Eq. (6), we used as before the expression for the ionization parameter $\xi = L/(n_H r^2)$. Plugging in typical values yields

$$\dot{M} \simeq 0.043 \frac{\Omega_{0.5} L_{43} v_{2000}}{\xi_4} M_\odot \text{yr}^{-1} \quad (7)$$

where v_{2000} is the outflow velocity in units of 2000 km s^{-1} , $\Omega_{0.5}$ is the opening solid angle as a fraction 0.5 of 4π str, and $\mu = 1.3$ is assumed. This mass loss rate needs to be further

suppressed in AGN feedback estimates, if the duty cycle of the flow over time (or effectively the radial volume filling factor) is substantially less than unity. The mass loss rate of eq. (7) implies kinetic power of $\dot{M}v^2/2 = 1.06 \times 10^{41} \text{ erg s}^{-1}$, which is two orders of magnitude less than $L_{\text{bol}} = 8 \times 10^{43} \text{ erg s}^{-1}$ (Reynolds et al. 1997). The outflow is more substantial in terms of momentum, as $(\dot{M}v)/(L_{\text{bol}}/c) \approx 0.4$. If the outflow is driven solely by radiation pressure then 80% of the radiation should be absorbed by the gas (a factor of 2 comes from the outflow opening angle compared with the bolometric 4π coverage). We find that the absorbed X-ray flux in our model is $\sim 26\%$. This value seems much lower than the 80% needed. However, the main radiation driven mechanism occurs in the UV band on which we do not have reliable data. Therefore, we cannot reach a clear conclusion, even though effective optical depth of 0.8 seems too high, at least in the X-ray band. The considerably less ionized state of the slow wind suggests it may carry much more mass than the fast component (eq. 7). However, the broad AMD of the slow component necessarily implies different physical conditions are present and a more complicated geometry than the simplified uniform, thin-shell picture assumed here for the fast component.

4.4. A Third, Local Absorption Component

In this section, we focus on the long wavelength region of the spectrum, which is filled predominantly with oxygen lines from highly ionized species down to neutral. Some of these lines have been ascribed, we believe erroneously, in previous works (Sako et al. 2003; Chelouche 2008) to the fast outflow. As demonstrated in §4.3, the absorption signature of the fast outflow at -1900 km s^{-1} actually diminishes rapidly with decreasing ξ . In fact, only the eight most highly ionized species show absorption at -1900 km s^{-1} .

The relevant part of the spectrum that is crowded with lines from neutral oxygen to O^{+6} is plotted in Fig. 4. Indeed, the numerous lines as well as the uncertainty associated with some of their wavelengths make the analysis of this spectral region particularly challenging. The top panel of Fig. 4 shows the model with absorption lines by the slow outflow (§4.2). Due to the low -100 km s^{-1} blueshift, these absorption lines lie just short of their rest-frame labels in the figure. Systematically blueshifted from these positions, additional absorption lines, not accounted for by the model in the upper panel, can be identified. These lines are shifted by $-2300 \pm 150 \text{ km s}^{-1}$. Above 20 \AA , this shift is readily discriminated by HETGS from the $-1900 \pm 150 \text{ km s}^{-1}$ velocity of the fast highly-ionized component. Furthermore, the oxygen lines in Fig. 4 are narrower than the relatively broad ($v_{\text{turb}} = 500 \text{ km s}^{-1}$) lines of the fast wind, which further precludes the oxygen lines from pertaining to the fast wind. On the other hand, a shift of -2300 km s^{-1} is exactly the cosmological redshift $z = 0.007749$

of MCG –6–30–15. Note that the spectrum in Fig. 4 has been de-redshifted to the AGN rest frame (as have been all other spectra plotted in this paper). Hence, lines that appear blueshifted by -2300 km s^{-1} are actually at rest in the local frame of reference. We therefore interpret these lines as arising locally from absorption by ionized ISM in our galaxy or in the Local Group at $z = 0$. The widths of the local oxygen absorption lines are not resolved here, but we use $v_{\text{turb}} = 100 \text{ km s}^{-1}$ to model the troughs and to obtain ionic column densities. This width is consistent with local, ionized ISM UV absorption lines at high resolution (Kaspi et al. 2004).

The lower panel in Fig. 4 shows the local $z = 0$ absorption component added to the model and it can be seen to provide a much improved fit and to account for most of the absorption that was missing in the model in the upper panel. We note that a few wavelengths had to be slightly corrected from their calculated value in order to fit the data. Wavelength adjustments facilitated by the HETGS spectrum are further discussed in §5. An exception to the good fit is the O^{+4} feature predicted at $\sim 22.17 \text{ \AA}$. It appears to be present in the data, but shifted by $\sim 0.2 \text{ \AA}$, or -300 km s^{-1} by comparison to the model. We checked whether this line could be due, alternatively, to absorption from excited, meta-stable levels of O^{+4} (Kaastra et al. 2004). However, the strongest such lines are expected at 22.488 \AA and at 22.453 \AA . Although there is some flux deficit in the spectrum around the latter position, it looks more like noise, and we find nothing that appears broad enough to be a conclusive absorption line (see Fig. 4). We conclude that the feature at 22.17 \AA cannot be explained by absorption from meta-stable levels.

The local column densities obtained from fitting the oxygen lines (Fig. 4) are listed in Table 7. The columns in the (slow) outflow component are also listed for comparison. It can be seen that neutral O, O^{+1} , O^{+5} , and O^{+6} are unambiguously detected. Local absorption by $\text{O}^{+2} - \text{O}^{+4}$ and by O^{+7} are less significant. The data around the leading $\text{K}\alpha$ lines of O^{+2} and O^{+3} are noisy (Fig. 4). O^{+4} appears to have a considerable absorption trough, but it does not exactly agree in position with the rest-frame wavelength. Local absorption in O^{+7} Ly α is blended with absorption in the fast component of that line. Indeed, we can only put an upper limit to the local component in O^{+7} of 10^{16} cm^{-2} . In fact, the Ly α line of O^{+7} has a different absorption profile than any other oxygen line from lower charge states, and is shown separately in Fig. 5. It can be clearly seen to have a broad and fast -1900 km s^{-1} component that is distinct from the local component. This result fits well with our assessment of the fast outflow being exclusively comprised of high ionization species, while the slow outflow and the local absorber are significantly less ionized. *IUE* spectra of MCG –6–30–15 show no flux below 3000 \AA which prohibits detection of oxygen lines in the UV.

Applying an ionization correction for the fractional abundances of $f_q \approx 0.5$ to the highest

column-density ion O^{+1} for which $N_{ion} = 10^{17} \text{ cm}^{-2}$, and then dividing by the solar O/H abundance (4.6×10^{-4}) yields a rough estimate to the equivalent hydrogen column density of $\sim 4 \times 10^{20} \text{ cm}^{-2}$, which is the same as the neutral column towards MCG –6–30–15, and for which our measurements now reveal an ionized phase. We can conclude there is roughly the same amount of ionized oxygen as neutral oxygen in the direction of MCG –6–30–15. Table 7 shows that while the slow component has very high column densities in the high charge states $O^{+5} - O^{+7}$, the column distribution of the local absorber is rather flat. The high intrinsic outflow columns are manifested in the prominent absorption from these ions, even in lines from relatively weak high-order transitions (Fig. 6). Conversely, high-order lines from the local component are inconspicuous and hardly detected. Spectral features due to dust grains with oxide composites may also be present in the data, but only to the extent that can explain the residuals to the atomic model plotted in Fig. 4.

5. Oxygen Wavelength Adjustments

Wavelengths of inner-shell absorption lines are obtained primarily from atomic computations and are difficult to benchmark in the laboratory. Two notable laboratory measurements relevant to inner-shell oxygen ions, albeit in emission, were published by Schmidt et al. (2004) and Gu et al. (2005). These measurements provide useful wavelengths of blends, even though some individual absorption lines remain hard to discern. The present HETGS spectrum of MCG –6–30–15 is of sufficiently high spectral resolution and S/N to be directly confronted with the computed wavelengths.

The published wavelengths for the leading $K\alpha$ absorption lines of O^{+4} and O^{+5} from laboratory measurements are 22.374 \AA and 22.019 \AA , respectively. Indeed, these wavelengths give a very good fit to the data with the outflow velocity of -100 km s^{-1} , which is prevalent throughout the slow outflow component (see Fig. 4). On the other hand, the computed positions of the corresponding higher order lines ($K\beta$, $K\gamma$, etc.) show slight discrepancies when compared with the observed absorption lines, as demonstrated in the upper panel of Fig. 6. This inconsistency can be remedied by adjusting the computed yet uncertain rest-frame wavelengths of these lines to match the observed absorption lines. The good agreement found for the leading $K\alpha$ lines makes the high-order wavelength adjustments independent of any kinematic uncertainty, since all lines of a given ion must be Doppler shifted by the exact same velocity. We invoke corrections of up to 45 m\AA to the computed wavelengths, which is comparable in magnitude to the maximal discrepancies found between HULLAC and measured wavelengths of the leading $K\alpha$ lines in laboratory measurements (Schmidt et al. 2004; Gu et al. 2005). The complete list of adjusted wavelengths is presented in Table 8. The

lower panel in Fig. 6 shows the best-fit model following the wavelength adjustments, which is clearly favored by the data. Note that the absorption line strengths (i.e., equivalent widths) have not changed much between the two panels of Fig. 6, as the ionic column densities are essentially anchored by the leading $K\alpha$ transitions (shown in Fig. 4).

Based on the observed spectrum around 23 Å (Fig. 4), we also inspect the leading $K\alpha$ lines and blends of $O^{+1} - O^{+3}$. The O^{+1} lines are better constrained by the deep trough of the local component, while the slow outflow component of this ion blends with local absorption by neutral O (see Fig. 4). The three strongest lines of O^{+1} are unresolved in the spectrum and require a uniform shift of +45 Å, which nicely produces the observed O^{+1} absorption trough. The significant improvement of the model following the wavelength adjustments is demonstrated in the bottom panel of Fig. 4. The O^{+2} and O^{+3} lines, both in the outflow and locally are rather weak in the spectrum. Consequently, although the computed wavelengths are likely somewhat inaccurate, reliable adjustments for these lines are unwarranted by the data. We set therefore the strongest O^{+2} line at 23.071 Å, which is the position of an (emission) line blend identified by Gu et al. (2005), and uniformly shift weaker HULLAC lines by the same amount (Table 8). For O^{+3} , we set the leading blend to 22.741 Å (again, an emission blend in Gu et al. 2005) and shift the other lines by the same amount with respect to their HULLAC positions. The summary of all adjusted wavelengths is given in Table 8.

The above improved wavelengths obtained from the HETGS spectrum of MCG –6–30–15 can be used for better line identification in other astrophysical absorption spectra. However, given the S/N and the uncertain conditions at the source, the new wavelengths should be trusted to no more than ± 10 mÅ. This calibration of wavelengths with HETGS can be viewed as a form of laboratory astrophysics from space. However, by no means can it replace actual absorption measurements carried out under controlled conditions in the laboratory.

6. CONCLUSIONS

We have analyzed the kinematic and thermal structure of the ionized outflow in MCG –6–30–15. We find three distinct absorption systems, two of which are intrinsic to the AGN. The slow component is outflowing at -100 km s^{-1} and spans a considerable range of ionization from neutral Fe to Fe^{+23} ($-1.5 < \log \xi < 3.5$ erg s^{-1} cm). A second, fast outflow component at -1900 km s^{-1} is very highly ionized ($\log \xi = 3.8$ erg s^{-1} cm). Finally, a third component of local absorption at $z = 0$ is detected for the first time in MCG –6–30–15 by its oxygen absorption.

Using our *AMD* reconstruction method for the slow component, we measured the distribution of column density as a function of ξ . We find a double-peaked distribution with a significant minimum at $0.5 < \log \xi < 1.5$ ($\text{erg s}^{-1} \text{cm}$), which corresponds to temperatures of $4.5 < \log T < 5$ (K). This minimum was observed in several other AGN outflows and it can be ascribed to thermal instability that appear to exist ubiquitously in photo-ionized Seyfert winds. The fast outflow with its narrow ionization distribution can be described as a thin shell and estimated to be approximately ten light days away from the central ionizing source. The local absorption system we believe could arise from either the ionized Galactic ISM, or from the Local Group. Finally, we use the HETGS spectrum to slightly improve on the computed wavelengths of the most important inner-shell O lines.

We thank Shai Kaspi and Doron Chelouche for useful discussions. TH and NA acknowledge support from *Chandra* grant AR-7 8011A. EB acknowledges funding from NASA grant 08-ADP08-0076.

REFERENCES

- Asplund, M., Grevesse, N., Sauval, A. J., & Scott, P. 2009, arXiv:0909.0948
- Badnell, N. R. 2006, *ApJ*, 651, L73
- Ballantyne, D. R., Vaughan, S., Fabian, A. C. 2003, *MNRAS*, 342, 239
- Bar-Shalom, A., Klapisch, M., & Oreg, J. 2001, *J. Quant. Spectr. Radiat. Transfer*, 71, 169
- Behar E., Cottam J C., & Kahn S. M. 2001, *ApJ*, 548, 966
- Behar, E., Sako, M., & Kahn S. M. 2001, *ApJ*, 563, 497
- Behar, E., & Netzer, H. 2002, *ApJ*, 570, 165
- Behar, E., Rasmussen, A. P., Blustin, A. J., Sako, M., Kahn, S. M., Kaastra, J. S., Branduardi-Raymont, G., & Steenbrugge, K. C. 2003, *ApJ*, 598, 232
- Bentz, M. C., Peterson, B. M., Netzer, H., Pogge, R. W., & Vestergaard, M. 2009, *ApJ*, 697, 160
- Blustin, A. J., Kriss, G. A., Holczer, T., Behar, E., & Kaastra, J. S. 2007, *A&A*, 466, 107
- Branduardi-Raymont, G., Sako, M., Kahn, S. M., Brinkman, A. C., Kaastra, J. S., & Page, M. J. 2001, *A&A*, 365, L140
- Chakravorty, S., Kembhavi, A. K., Elvis, M., Ferland, G. 2009, *MNRAS*, 393, 83
- Chelouche, D., astro-ph/arXiv:0812.3621v1
- Crenshaw, D. M., Kraemer, S. B., George, I. M., 2003, *ARA&A*, 41, 117
- Decaux, V., Beiersdorfer, P., Osterheld A., Chen M., & Kahn, S. M. 1995, *ApJ*, 443, 464
- Decaux, V., Beiersdorfer, P., Kahn, S. M., & Jacobs, V. L. 1997, *ApJ*, 482, 1076
- Dickey, J. M., Lockman, F. J. 1990, *ARA&A* 28, 215
- Fabian, A. C. et al., 1994, *PASJ*, 46, L59
- Fisher, K. B., Huchra, J. P., Strauss, M. A., Davis, M., Yahil, A., Schlegel, D., 1995, *ApJS*, 100, 69
- Gonçalves, A. C., Collin, S., Dumont, A. M., & Chevallier, L., 2007, *A&A*, 465, 9G

- Gu, M. F., Schmidt, M., Beiersdorfer, P., Chen, H., Thorn, D. B., Träbert, E., Behar, E., & Kahn, S. M. 2005, *ApJ*, 627, 1066
- Gu, M. F., Holczer, T., Behar, E., & Kahn, S. M. 2006, *ApJ*, 641, 1227
- Halpern, J., P., 1984, *ApJ*, 281, 90
- Hess, C. J., Kahn, S. M., & Paerels, F. B. S. 1997, *ApJ*, 478, 94
- Holczer, T., Behar, E., & Kaspi, S. 2005, *ApJ*, 632, 788
- Holczer, T., Behar, E., & Kaspi, S. 2007, *ApJ*, 663, 799
- Kaastra, J. S., et al. 2004, *A&A*, 428, 57
- Kallman, T. R., & Bautista, M. 2001, *ApJS*, 133, 221
- Kaspi, S., Smith P., Netzer N., Maoz D., Jannuzi B. T. & Giveon U. 2000, *ApJ*, 533, 631
- Kaspi et al. 2001, *ApJ*, 554, 216
- Kaspi, S., Brandt, W. N., Collinge, M. J., Elvis, M., & Reynolds, C. S. 2004, *AJ*, 127, 2631
- Kinkhabwala, A., et al. 2002, *ApJ*, 575, 732
- Krolik, J. H., McKee, C. F., Tarter, C. B. 1981, *ApJ*, 249, 422
- Lee, J. C., et al. 2001, *ApJ*, 554, L13
- Lee, J. C., Xiang, J., Ravel, B., Kortright, J., & Flanagan, K. 2009, astro-ph/arXiv:0906.3720
- McKernan, B., Yaqoob, T. & Reynolds, C. S. 2007, *MNRAS*, 379, 1359
- Miller, L., Turner, T. J., & Reeves, J. N. 2008, *A&A*, 483, 437
- Netzer, H. 2004, *ApJ*, 604, 551
- Otani, C., et al. *PASJ*, 48, 211
- Reynolds, C. S., Fabian, A. C., Nandra, K., Inoue, H., Kunieda, H., & Iwasawa, K. 1995, *MNRAS*, 277, 901
- Reynolds, C. S., Ward, M., J., Fabian, A., C. & Celotti, A. 1997, *MNRAS*, 291, 403
- Sako, M. et al. 2001, *A&A*, 365, L168
- Sako, M. et al. 2003, *ApJ*, 596, 114

Schmidt, M., Beiersdorfer, P., Chen, H., Thorn, D. B., Träbert, E. & Behar, E. 2004, ApJ, 604, 562

Steenbrugge, K. C. et al. 2005, A&A, 432, 453

Tanaka, Y., et al.. 1995, Nature, 375, 659

Turner, A. K., Fabian, A. C., Lee, J. C., & Vaughan, S. 2004, MNRAS, 353, 319

Young, A. J., Lee, J. C., Fabian, A. C., Reynolds, C. S., Gibson, R. R., & Canizares, C. R. 2005, ApJ, 631, 733

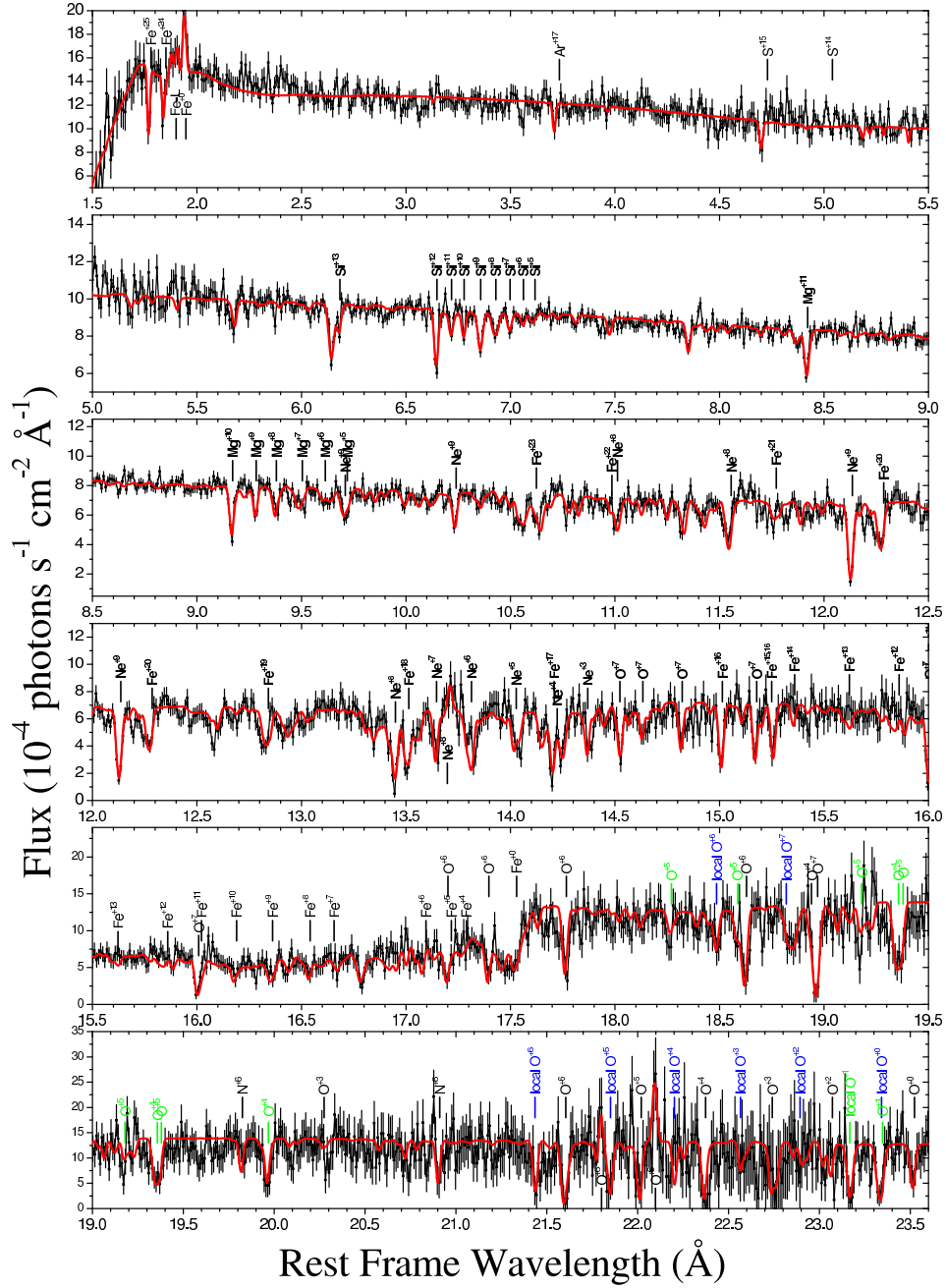


Fig. 1.— *Chandra* HETGS spectrum of MCG -6-30-15 corrected for cosmological redshift ($z = 0.007749$). Top panel includes only HEG data, while all other panels present the combined MEG+HEG spectrum. The red line is the best-fit model including the slow (§4.2) and fast (§4.3) outflow components as well as the local $z = 0$ component (§4.4). Ions producing the strongest absorption (emission) lines and blends are marked above (below) the data. Oxygen lines that require slight wavelength adjustments are marked in green.

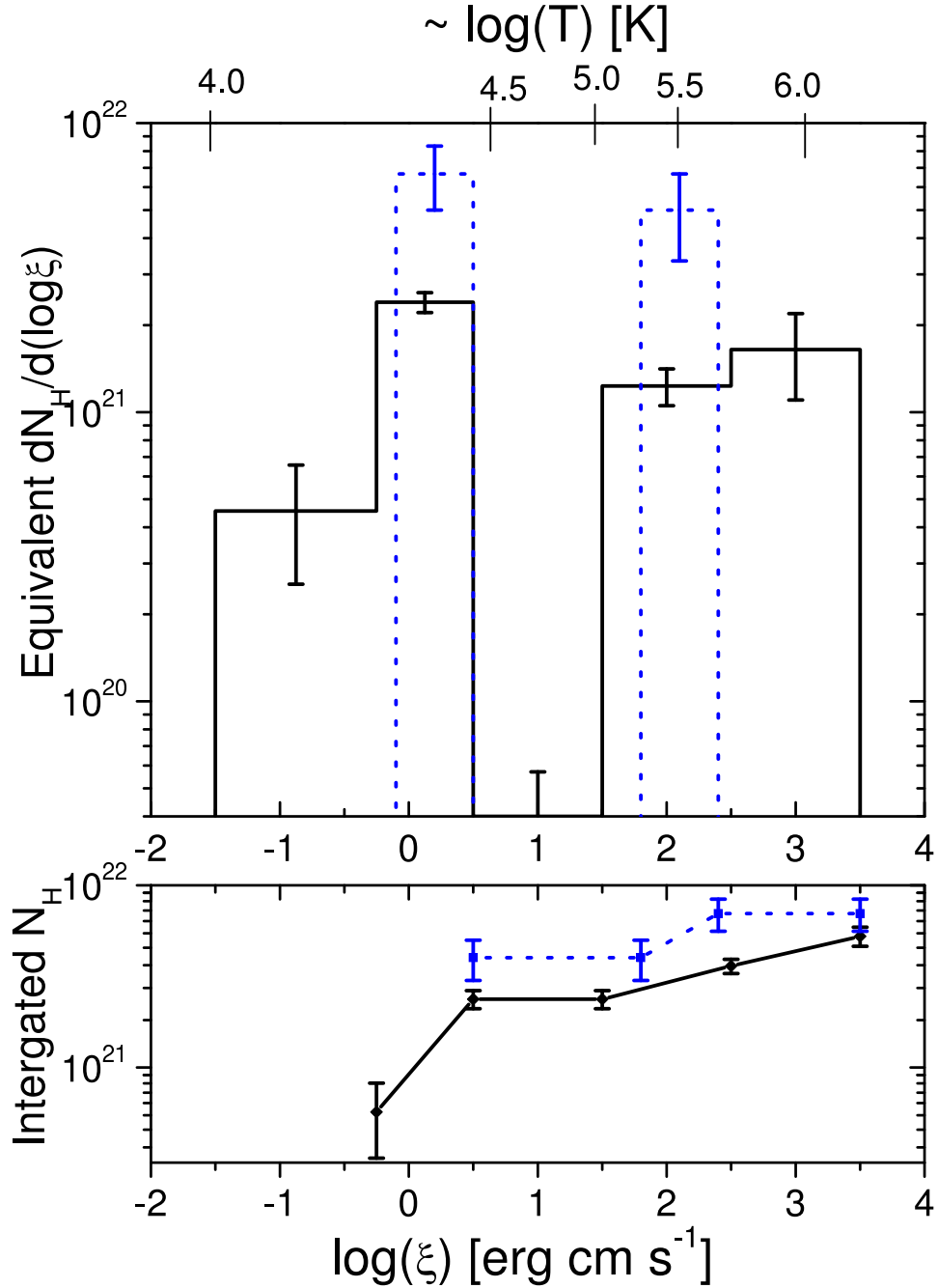


Fig. 2.— AMD of the slow outflow in MCG -6-30-15 obtained exclusively from Fe absorption and scaled by the solar Fe/H abundance 3.16×10^{-5} (Asplund et al. 2009). The corresponding temperature scale, obtained from the XSTAR computation is shown at the top of the figure. The middle bin value is zero, and only the upper limit uncertainty is plotted. The cumulative column density up to ξ is plotted in the lower panel, yielding a total of $N_H = (5.3 \pm 0.7) \times 10^{21}$ cm $^{-2}$. (Dotted) blue lines represent the two ionization components of McKernan et al. (2007) broadened by their 3σ uncertainty of $\Delta\xi = 0.3$ erg s $^{-1}$ cm. The cumulative column density of McKernan et al. (2007) is plotted as a blue line in the lower

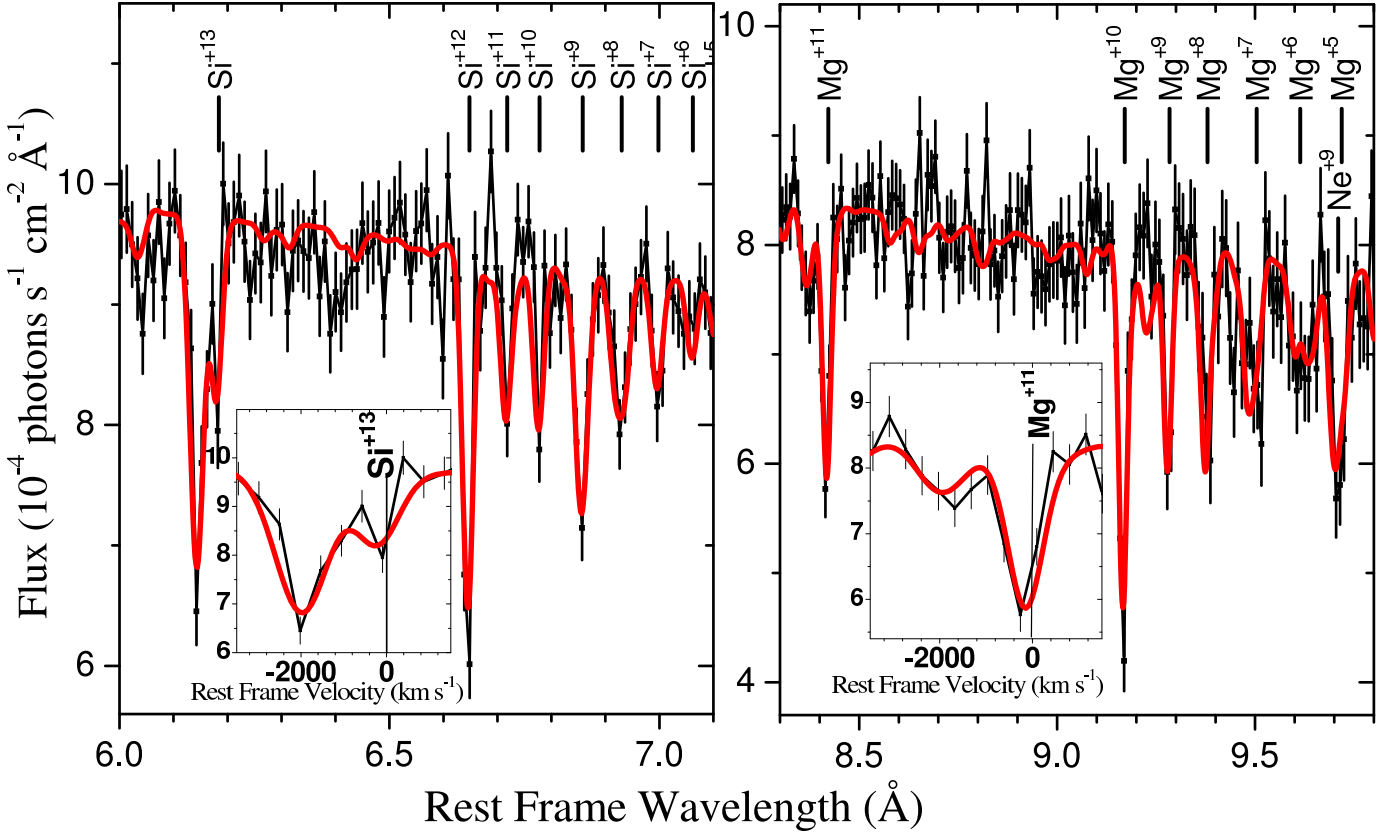


Fig. 3.— Extract from the HETGS spectrum of MCG –6–30–15 corrected for cosmological redshift ($z = 0.007749$). The red line is the best-fit model including the slow (-100 km s^{-1}) and fast (-1900 km s^{-1}) outflow components. (*left*) Si^{+13} through Si^{+6} absorption. Only H-like Si^{+13} shows a fast component. (*right*) Mg^{+11} through Mg^{+5} absorption. H-like Mg^{+11} shows a fast component, but a much more prominent slow component. Lower charge states show only the slow component. The insets show the two H-like lines in velocity space. The plot demonstrates the low ionization cutoff in the fast component, which is manifested by only the most ionized species.

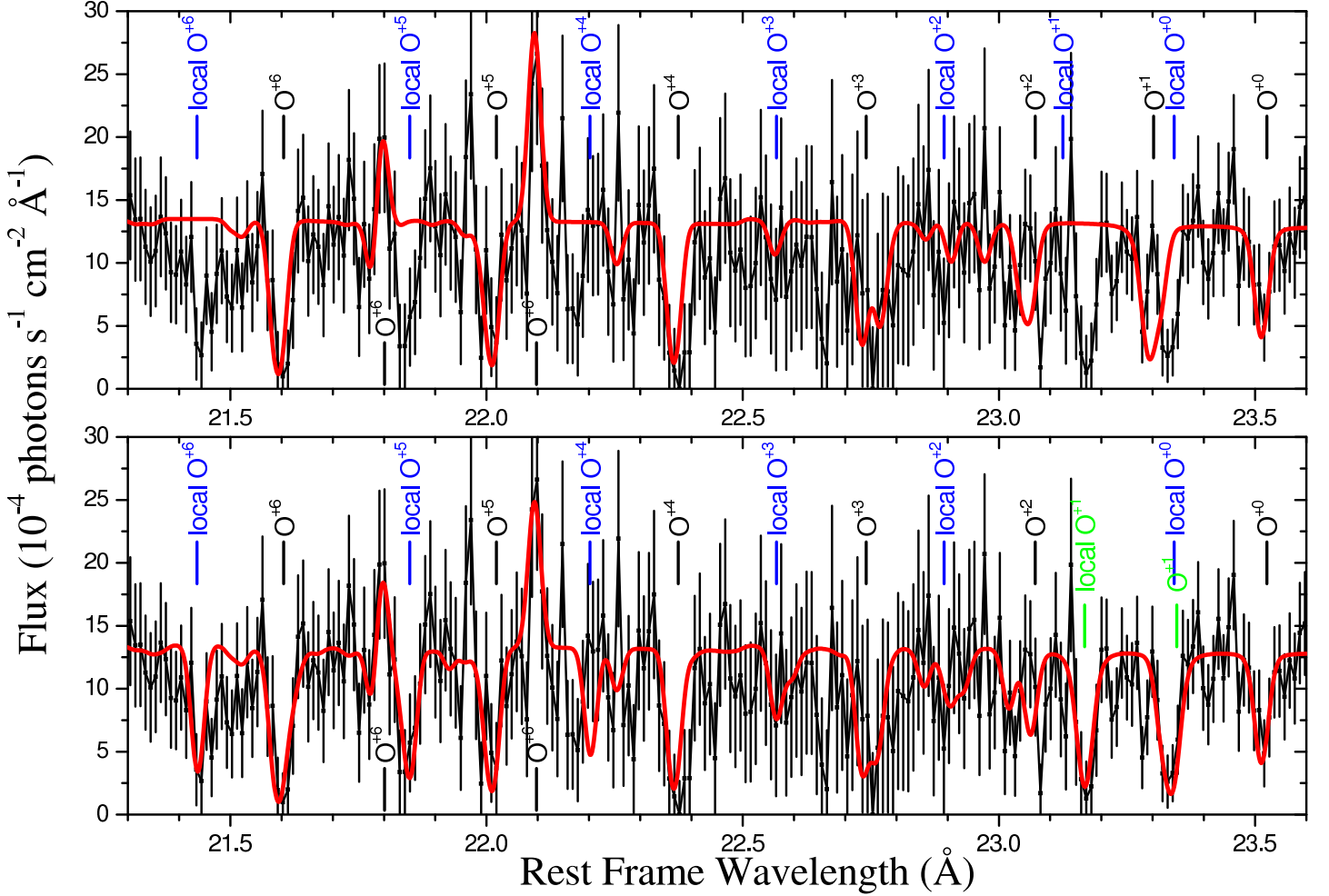


Fig. 4.— Oxygen K α line region of the HETGS spectrum of MCG -6-30-15 corrected for cosmological redshift ($z = 0.007749$). Red curve indicates model. Most important lines are labeled at their rest frame. Labels "local" refer to positions expected for the $z = 0$ absorber. Green labels refer to adjusted wavelengths (§5). (*top*) Model includes only AGN (mostly slow ~ 100 km s^{-1}) outflow. (*low*) Improved model includes also local absorption.

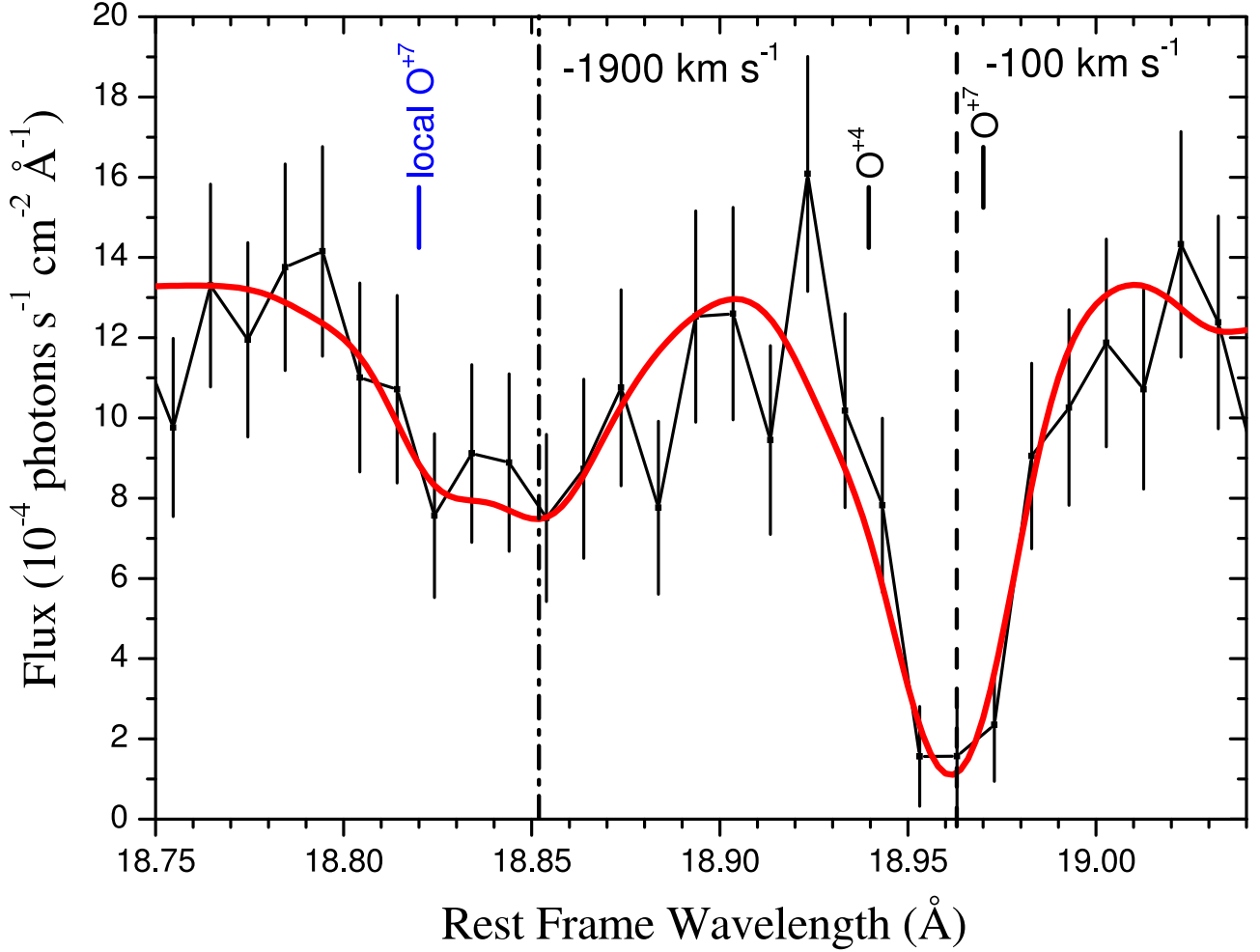


Fig. 5.— HETGS spectrum of MCG -6-30-15 corrected for cosmological redshift ($z = 0.007749$) around the prominent O^{+7} Ly α line. The red line is the (globally) best-fit model. Absorption by both slow (-100 km s^{-1}) and fast (-1900 km s^{-1}) components are clearly discerned (unlike lower oxygen charge states in Fig. 4 that have only a slow component). The fast component is also broader ($v_{\text{turb}} = 500 \text{ km s}^{-1}$) than the unresolved slow one ($v_{\text{turb}} = 100 \text{ km s}^{-1}$ further broadened by the instrument). The marginally detected local-component line is also indicated.

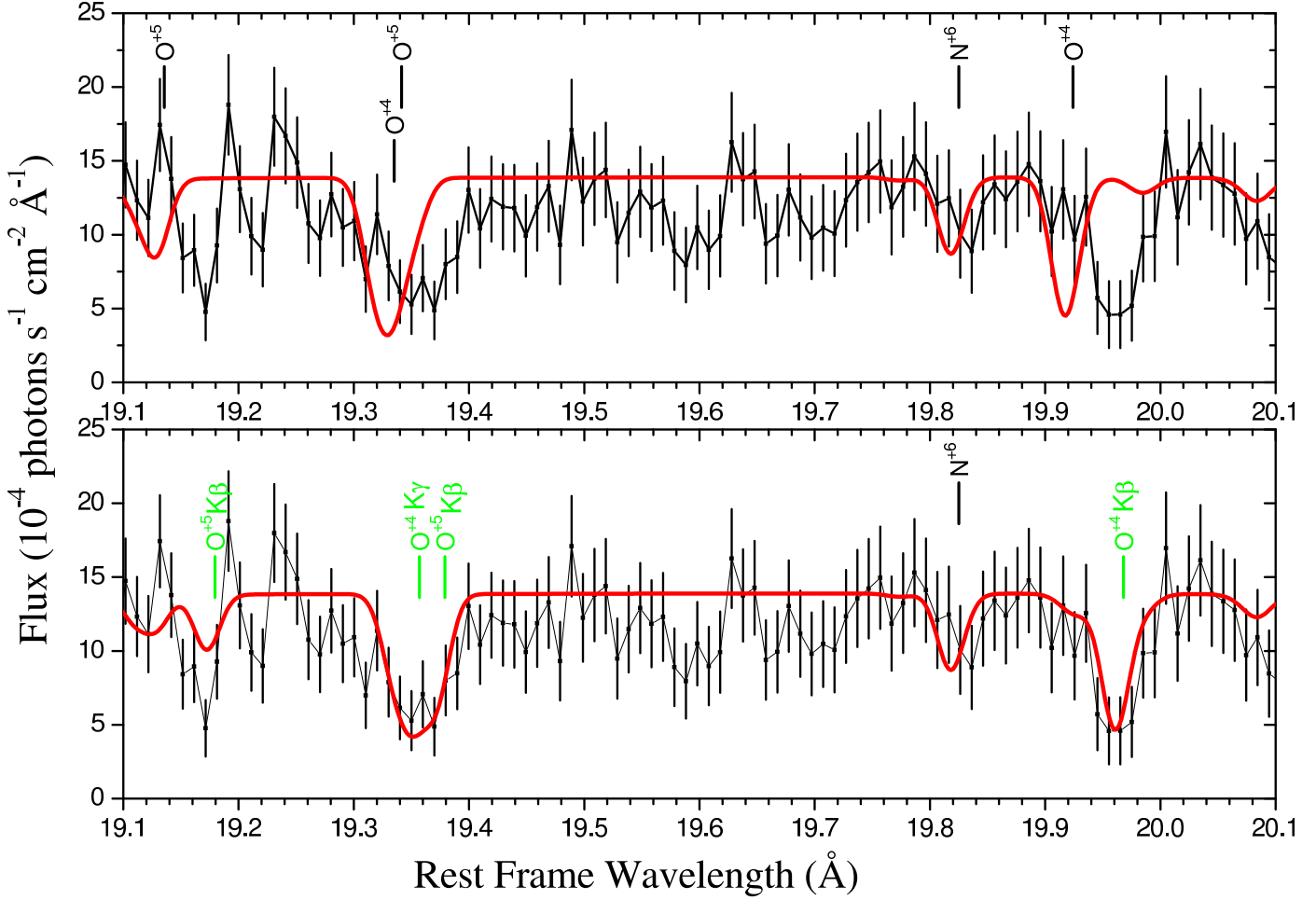


Fig. 6.— Extract from HETGS spectrum of MCG -6-30-15 corrected for cosmological redshift ($z = 0.007749$) demonstrating the ability of HETGS to accurately calibrate rest-frame wavelengths. The red lines represent the model with the -100 km s^{-1} blueshift of the slow wind. (*top*) Model using HULLAC computed wavelengths. (*bottom*) Improved model using re-calibrated wavelengths.

Table 1. Historical observations of the ionized absorber in MCG –6–30–15

Observatory	Year	Duration (ks)	Flux level at 1 keV (10^{-3} ph cm $^{-2}$ s $^{-1}$ keV $^{-1}$)	References ^a
<i>ROSAT</i>	1992	8.5	6	1
<i>ASCA</i>	1994	150	9	1, 2
<i>Chandra</i>	2000	120	10	4, 7
<i>XMM-Newton</i>	2000	120	6	3, 5, 8
<i>XMM-Newton</i>	2001	320	9	6, 8
<i>Chandra</i>	2004	520	10	8, 9, 10
<i>Suzaku</i>	2006	250	8	8

^a 1. Reynolds et al. (1997), 2. Otani et al. (1996), 3. Branduardi-Raymont et al. (2001), 4. Lee et al. (2001), 5. Sako et al. (2003), 6. Turner et al. (2004), 7. McKernan et al. (2007), 8. Miller et al. (2008), 9. Chelouche (2008), 10. present work.

Table 2. *Chandra* observations of MCG –6–30–15 used in this work

Obs. ID	Start Date	Detector	Gratings	Exposure (s)	Counts in HEG orders \pm 1	Counts in MEG orders \pm 1
4760	2004 May 19	ACIS-S	HETG	169590	50630	107040
4761	2004 May 21	ACIS-S	HETG	156230	51279	109923
4759	2004 May 24	ACIS-S	HETG	158535	50152	108233
4762	2004 May 27	ACIS-S	HETG	37549	13637	28289

Table 3. Narrow Emission Lines

Line	λ_{Rest} (Å)	$\lambda_{\text{Observed}}^{\text{a}}$ (Å)	Flux (10^{-5} photons s^{-1} cm^{-2})
$\text{Fe}^{+0} - \text{Fe}^{+9} \text{K}\alpha$	1.94	$1.940 \pm 0.006^{\text{b}}$	1.0 ± 0.2
$\text{Fe}^{+10} - \text{Fe}^{+16} \text{K}\alpha$	$1.93 - 1.94^{\text{d}}$	$1.905 \pm 0.006^{\text{b}}$	0.5 ± 0.1
$\text{Fe}^{+17} - \text{Fe}^{+23} \text{K}\alpha$	$1.86 - 1.90^{\text{e}}$	$1.877 \pm 0.006^{\text{b}}$	0.4 ± 0.1
Ne^{+8} forbidden	13.698	$13.710 \pm 0.012^{\text{c}}$	0.5 ± 0.1
O^{+6} intercombination	21.801	$21.794 \pm 0.009^{\text{c}}$	3.5 ± 0.6
O^{+6} forbidden	22.097	$22.093 \pm 0.009^{\text{c}}$	6 ± 1

^a in the AGN rest frame.

^b FWHM = 15 mÅ.

^c FWHM = 235 km s^{-1} .

^d Decaux et al. (1995).

^e Decaux et al. (1997).

Table 4. Current best-fit column densities for ions detected in the 2004 HETGS spectrum of MCG –6–30–15 compared with the 2000 RGS spectrum (Sako et al. 2003).

Ion	HETGS		RGS		Ion	HETGS		RGS	
	N_{ion} (10^{16} cm $^{-2}$)		N_{ion} (10^{16} cm $^{-2}$)			N_{ion} (10^{16} cm $^{-2}$)		N_{ion} (10^{16} cm $^{-2}$)	
	Slow	Fast	Slow	Fast		Slow	Fast	Slow	Fast
N ⁺⁶	10^{+8}_{-3}	...	3.7	1.3	Si ⁺¹¹	$2.0^{+0.2}_{-1.5}$	
O ⁺⁰	10^{+5}_{-5}	Si ⁺¹²	$12.0^{+1.5}_{-3.5}$...	≤ 12.6 ^a	3.3
O ⁺¹	8^{+16}_{-1}	Si ⁺¹³	$3.0^{+0.5}_{-1.0}$	$8^{+0.5}_{-1}$	≤ 10.7 ^a	≤ 34.7 ^a
O ⁺²	$1.0^{+2.0}_{-0.5}$	S ⁺¹⁵	...	$6^{+5.4}_{-1.1}$
O ⁺³	$6^{+12}_{-0.6}$	Ar ⁺¹⁷	...	$8^{+3.2}_{-2.4}$
O ⁺⁴	12^{+3}_{-5}	...	$8.7 \leq 1.6$ ^a	...	Fe ⁺⁰ ^e	$5^{+1}_{-0.6}$
O ⁺⁵ ^b	$12^{+1.5}_{-6}$...	3.6	1.0	Fe ⁺¹	$4^{+1}_{-0.8}$
O ⁺⁶ ^c	$60^{+7.5}_{-6}$...	22	1.4	Fe ⁺²	$0.5^{+0.3}_{-0.5}$
O ⁺⁷ ^d	120^{+12}_{-24}	$2^{+1.6}_{-0.3}$	19	5.6	Fe ⁺³	$0.5^{+0.5}_{-0.5}$
Ne ⁺³	$2^{+5}_{-0.8}$	Fe ⁺⁴	$0.6^{+0.2}_{-0.6}$
Ne ⁺⁴	$4^{+3.4}_{-0.6}$	Fe ⁺⁵	$0.7^{+0.2}_{-0.7}$
Ne ⁺⁵	$4^{+6}_{-0.6}$	Fe ⁺⁶	$0.7^{+0.2}_{-0.7}$
Ne ⁺⁶	$2.5^{+0.2}_{-1.6}$	Fe ⁺⁷	$1^{+0.1}_{-0.8}$
Ne ⁺⁷	$6^{+0.8}_{-2}$	Fe ⁺⁸	$0.7^{+0.2}_{-0.2}$
Ne ⁺⁸	10^{+1}_{-5}	...	3.5	1.2	Fe ⁺⁹	$1.2^{+0.6}_{-0.1}$
Ne ⁺⁹	20^{+2}_{-7}	...	10	6.6	Fe ⁺¹⁰	$1.5^{+0.1}_{-0.6}$
Mg ⁺⁴	$0.5^{+0.3}_{-0.5}$	Fe ⁺¹¹	$1.2^{+0.1}_{-1.1}$
Mg ⁺⁵	$0.5^{+0.4}_{-0.5}$	Fe ⁺¹²	$0.5^{+0.1}_{-0.4}$
Mg ⁺⁶	$2.0^{+0.2}_{-1.6}$	Fe ⁺¹³	$0.2^{+0.1}_{-0.1}$
Mg ⁺⁷	$1.5^{+0.3}_{-0.7}$	Fe ⁺¹⁴	$0.2^{+0.05}_{-0.2}$
Mg ⁺⁸	$2.0^{+0.2}_{-1.8}$	Fe ⁺¹⁵	$0.5^{+0.1}_{-0.3}$
Mg ⁺⁹	$2.0^{+0.2}_{-1.6}$	Fe ⁺¹⁶	$3^{+0.3}_{-1.9}$...	2.6	0.5
Mg ⁺¹⁰	$8.0^{+0.8}_{-2.7}$...	1.3	1.4	Fe ⁺¹⁷	$4.5^{+0.5}_{-2.1}$...	9.3	2.4
Mg ⁺¹¹	$4.0^{+0.4}_{-1.4}$	$1.2^{+0.2}_{-0.6}$	≤ 5.5 ^a	5.4	Fe ⁺¹⁸	$4^{+0.4}_{-1.4}$...	10.5	2.4
Si ⁺⁵	$0.5^{+1.0}_{-0.5}$	Fe ⁺¹⁹	$1.5^{+0.1}_{-0.7}$...	3.1	6.5
Si ⁺⁶	$2.5^{+1.0}_{-0.9}$	Fe ⁺²⁰	$1^{+0.1}_{-0.8}$...	5.4	8.9
Si ⁺⁷	$2.5^{+2.0}_{-0.5}$	Fe ⁺²¹	$1^{+0.1}_{-0.9}$...	4.6	4.9
Si ⁺⁸	$3.5^{+0.5}_{-1.0}$	Fe ⁺²²	$1^{+0.1}_{-0.9}$...	0.1	10.1
Si ⁺⁹	$4.0^{+0.6}_{-0.4}$	Fe ⁺²³	$0.5^{+0.4}_{-0.4}$	$3^{+0.5}_{-3}$	2.6	≤ 4.1 ^a
Si ⁺¹⁰	$2.0^{+0.2}_{-1.4}$	Fe ⁺²⁴ ^f	...	60^{+13}_{-26}
					Fe ⁺²⁵ ^f	...	120^{+52}_{-28}

^a 90% upper limit.

^b Lee et al. (2001) quote $N_{O+5} \approx 3 \times 10^{17}$ cm $^{-2}$ in the slow component.

^c Lee et al. (2001) quote $N_{O+6} \geq 7 \times 10^{17}$ cm $^{-2}$ from absorption lines and $N_{O+6} \approx 2.5 \times 10^{18}$ cm $^{-2}$ from the edge drop. Turner et al. (2004) quote $N_{O+6} \approx 2 - 8 \times 10^{18}$ cm $^{-2}$. Both refer to the slow component.

^d Lee et al. (2001) quote $N_{O+7} \approx 10^{18}$ cm $^{-2}$ from the edge drop. Turner et al. (2004) quote $N_{O+7} \approx 2.5 - 3 \times 10^{18}$ cm $^{-2}$. Both refer to the slow component.

^e Lee et al. (2001) quote $N_{Fe+0} \approx 4 \times 10^{17}$ cm $^{-2}$ in the slow component from edge drop.

Table 5. Physical Parameters for The Slow Component: Comparison.

Reference	Column Density (10^{21} cm^{-2})	Outflow Velocity (km s^{-1})	$v_{\text{turb}}(b)$ (km s^{-1})	Ionization Parameter $\log\xi$ ($\text{erg s}^{-1} \text{ cm}$)
Otani et al. (1996)	4.6	1.2
	13	1.9
Reynolds et al. (1997)	5	1.3
	13	1.9
Lee et al. (2001)	5	...	100	1.2
	30	...	100	1.9
Sako et al. (2003)	2 ^a	-150 ± 130	130	0.5 – 2
Turner et al. (2004)	...	80 ± 260	50 – 150	...
McKernan et al. (2007)	3 ± 1	<30	170	0.2 ± 0.1
	4 ± 1	<15	170	2.1 ± 0.1
Miller et al. (2008)	0.22 ± 0.01	-0.04 ± 0.16
	1.1 ± 0.8	2.33 ± 0.05
Chelouche (2008)	...	~ -150 ^b	...	0.8 – 3.1
Present Work	2.3 ± 0.3	-100 ± 50	100	-1.5 – 0.5
	3.0 ± 0.4	-100 ± 50	100	1.5 – 3.5

^a Sako et al. (2003) used twice solar Fe abundance in order to derive equivalent hydrogen column.

^b See Fig. 16 in Chelouche (2008).

Table 6. Physical parameters of the fast component: Comparison

Reference	Column Density (10^{21} cm^{-2})	Outflow Velocity (km s^{-1})	$v_{\text{turb}}(b)$ (km s^{-1})	Ionization Parameter $\log\xi$ ($\text{erg s}^{-1} \text{ cm}$)
Sako et al. (2003)	2 ^a	-1900 ± 140	460	2 – 3
Turner et al. (2004)	...	-1970 ± 160	50 – 150	...
Young et al. (2005)	20 – 150 ^b	-2000^{+700}_{-900}	100 – 500 ^b	$3.6^{+0.1}_{-0.2}$
McKernan et al. (2007)	30^{+60}_{-20}	-1550^{+80}_{-150}	170	$3.7^{+0.1}_{-0.3}$
Miller et al. (2008)	21	-1800	500	3.85
Chelouche (2008)	...	-2000	...	0.3 – 3.8
Present Work	81 ± 7	-1900 ± 150	500	3.82 ± 0.03

^a Sako et al. (2003) used Fe abundance twice solar to derive equivalent hydrogen column.

^b Young et al. (2005) derive two possible columns depending on v_{turb} . They quote $N_H \sim 2 - 4 \times 10^{22} \text{ cm}^{-2}$ for $v_{\text{turb}} = 500 \text{ km s}^{-1}$ and $N_H \sim 1.5 \times 10^{23} \text{ cm}^{-2}$ for $v_{\text{turb}} = 100 \text{ km s}^{-1}$.

Table 7. Oxygen ionic column densities in the local ($z = 0$) absorbing component. Respective columns in the slow outflow intrinsic to MCG –6–30–15 are listed for comparison. See Fig. 4 for the relevant spectrum.

Charge State	N_{ion} local (10^{16} cm^{-2})	Leading $K\alpha$ line/blend λ_{Rest} (\AA)	$\lambda_{\text{Observed}}^{\text{a}}$ (\AA)	N_{ion} intrinsic (10^{16} cm^{-2})
neutral O ^b	4_{-4}^{+8}	23.523	23.509	10_{-5}^{+5}
O ⁺¹	10_{-2}^{+20}	23.347 ^c	23.350	8_{-1}^{+16}
O ⁺²	$1_{-0.7}^{+2}$	23.071 ^c	23.065	$3_{-0.5}^{+6}$
O ⁺³	1_{-1}^{+2}	22.741 ^c	22.739	$6_{-0.6}^{+12}$
O ⁺⁴	2_{-1}^{+2}	22.374 ^c	22.345	12_{-5}^{+3}
O ⁺⁵	4_{-1}^{+2}	22.019 ^c	22.003	$12_{-6}^{+1.5}$
O ⁺⁶	4_{-1}^{+2}	21.602	21.605	$60_{-6}^{+7.5}$
O ⁺⁷	<1	18.969	18.973	120_{-24}^{+12}

^a Uncertainty of $\pm 10 \text{ m\AA}$.

^b Strong overlap with intrinsic O⁺¹, see Fig. 4.

^c Adjusted to fit data. See §5 and Table 8.

Table 8. Rest frame wavelengths of oxygen absorption lines and blends determined from HETGS spectrum

Ion; Lines	Transition ^a		<i>f</i> -value	λ_{HULLAC} (Å)	λ_{HETGS} ^b (Å)	$\Delta\lambda$ (mÅ)
	Ground Configuration (J)	Upper Configuration (J)				
O ⁺¹ K α ^c	1s ² 2s ² 2p _{1/2} 2p _{3/2} ² (J = 3/2)	1s2s ² 2p _{1/2} ² 2p _{3/2} ² (J = 5/2)	0.100	23.302	23.347	+45
		1s2s ² 2p _{1/2} 2p _{3/2} ³ (3/2)	0.067	23.300	23.345	
		1s2s ² 2p _{3/2} ⁴ (1/2)	0.034	23.300	23.345	
O ⁺² K α ^c	1s ² 2s ² 2p _{1/2} ² (0)	1s2s ² [2p _{1/2} ² 2p _{3/2} + 2p _{3/2} ³] (1)	0.125	23.108	23.071 ^e	–37
		1s2s ² [2p _{1/2} 2p _{3/2} ² + 2p _{3/2} ³] (1)	0.104	23.065	23.028	
		1s2s ² [2p _{1/2} 2p _{3/2} ² + 2p _{1/2} ² 2p _{3/2}] (1)	0.069	22.977	22.940	
O ⁺³ K α ^c	1s ² 2s ² 2p _{1/2} (1/2)	1s2s ² [2p _{1/2} 2p _{3/2} + 2p _{1/2} ²] (1/2)	0.167	22.749	22.741 ^e	–8
		1s2s ² [2p _{1/2} 2p _{3/2} + 2p _{3/2} ²] (3/2)	0.077	22.747		–6
O ⁺³ K α		1s2s ² [2p _{1/2} 2p _{3/2} + 2p _{3/2} ²] (3/2)	0.142	22.777	22.770	–7
O ⁺⁴ K α	1s ² 2s ² (0)	1s2s ² 2p _{3/2} (1)	0.539	22.337	22.374 ^e	+37
O ⁺⁴ K β		1s2s ² 3p _{3/2} (1)	0.112	19.924	19.968	+44
O ⁺⁴ K γ		1s2s ² 4p _{3/2} (1)	0.046	19.324	19.357	+33
O ⁺⁵ K α ^c	1s ² 2s (1/2)	1s2s2p _{3/2,1/2} (3/2, 1/2)	0.349, 0.173	22.013	22.019 ^d	+6
O ⁺⁵ K β ^c		1s2s3p _{3/2} (3/2, 1/2)	0.064, 0.032	19.341	19.379	+38
O ⁺⁵ K β ^c		1s2s3p _{3/2,1/2} (3/2, 1/2)	0.025, 0.012	19.136	19.180	+44
O ⁺⁵ K γ ^c		1s2s4p _{3/2} (3/2, 1/2)	0.027, 0.014	18.606	18.587	–19
O ⁺⁵ K δ ^c		1s2s5p _{3/2} (3/2, 1/2)	0.015, 0.007	18.290	18.270	–20

^a Square brackets indicate significant configuration mixing.

^b With an accuracy of ± 10 mÅ.

^c Unresolved blend shifted uniformly.

^d Schmidt et al. (2004) give 22.019 ± 0.003 Å for this line.

^e Gu et al. (2005) report blends at 22.374 ± 0.003 Å, 22.741 ± 0.004 Å, and 23.071 ± 0.004 Å that include, respectively, the relevant O⁺⁴, O⁺³, and O⁺² K α lines.